J Therm Anal Calorim (2009) 98:409–421
DOI 10.1007/s10973-009-0295-x

Synthesis, characterization and thermal behaviour of new copper and rare-earth metal tungstates

E. Tomaszewicz · J. Typek · S. M. Kaczmarek

Received: 1 October 2008 / Accepted: 2 February 2009 / Published online: 7 August 2009

Abstract Three series of new copper and rare-earth metal tungstates with the formulas: $CuRE_2W_2O_{10}$ (RE = Nd, Sm, Eu) and $Cu_3RE_2W_4O_{18}$ (RE = Sm, Eu or RE = Dy, Ho, Er) were synthesized by the solid-state reaction method. The $CuRE_2W_2O_{10}$ and $Cu_3RE_2W_4O_{18}$ (RE = Dy, Ho, Er) compounds crystallize in the monoclinic system. The $Cu_3RE_2W_4O_{18}$ phases with the large rare-earth ions crystallize in the triclinic system. All obtained compounds melt incongruently below 1273 K. The anion lattice of the $Cu_3RE_2W_4O_{18}$ phases is built from isolated groups of octahedra $(W_4O_{16})^{8-}$, while $CuRE_2W_2O_{10}$ from WO_6 octahedra forming structural elements $[(W_2O_9)^{6-}]^{\infty}$. The EPR spectra of analyzed compounds consisted of an intense line originating generally from the rare-earth ions and a weak, narrow line from Cu^{2+} separate centers appearing only on the surface of the grains. The absence of bulk copper in the EPR spectrum is probably due to a very short relaxation time of the Cu^{2+} subsystem.

Keywords Copper tungstate · Rare-earths tungstates · DTA-TG · IR · EPR

E. Tomaszewicz (✉)
Department of Inorganic and Analytical Chemistry,
West Pomeranian University of Technology,
Al. Piastow 42, 71-065 Szczecin, Poland
e-mail: tomela@ps.pl

J. Typek · S. M. Kaczmarek
Institute of Physics, West Pomeranian University of Technology,
Al. Piastow 17, 70-310 Szczecin, Poland

Introduction

Copper tungstate belongs to the triclinic distorted wolframite type structure [1–3] in which every metal ion is surrounded by six oxygen ions (the six M–O distances are within the range of 0.1961–0.2450 nm for CuO_6 octahedra and within the range of 0.1760–0.2208 nm for WO_6 octahedra [1]). The crystal structure of $CuWO_4$ can be described as a hexagonal close-packing framework of oxygen ions with Cu^{2+} and W^{6+} ions occupying half of the octahedral sites [1, 4]. Copper tungstate has a potential technological significance in such applications as: scintillation detectors, optical fibres, laser materials and photoanodes [5–7]. On the other hand, rare-earth double tungstates or molybdates (particularly with alkali ions, e.g. $ARE(WO_4)_2$ A = Na, K; RE = Y, Gd) are known as promising host materials for luminescent applications [8–14]. These compounds doped by other trivalent rare-earth ions (Nd^{3+}, Eu^{3+}, Yb^{3+}, Er^{3+}) have been widely used in cathodoluminescent display phosphor screens, solid-state lasers, electroluminescent optical devices and probes because their luminescence exhibits high fluorescent efficiency, very sharp emission bands and excellent monochromatocity [8–14]. Motivated by very interesting properties of new rare-earths compounds we have investigated mutual reactivity of $CuWO_4$ with rare-earth metal tungstates in order obtaining of new compounds for industrial applications.

Our earlier studies concerning the reactivity in the solid state between $CuWO_4$ and Gd_2WO_6 showed that both reagents enter into reaction to give two unknown up to now phases: $Cu_3Gd_2W_4O_{18}$ and $CuGd_2W_2O_{10}$ [15]. Both compounds were synthesized by means of a conventional ceramic method according to the following reactions [15]:

$$3CuWO_{4(s)} + Gd_2WO_{6(s)} = Cu_3Gd_2W_4O_{18(s)} \quad (1)$$

$$CuWO_{4(s)} + Gd_2WO_{6(s)} = CuGd_2W_2O_{10(s)} \quad (2)$$

$Cu_3Gd_2W_4O_{18}$ crystallizes in the triclinic system and melts incongruently at 1173 K [15]. The $CuGd_2W_2O_{10}$ compound crystallizes in the monoclinic system and melts incongruently at 1248 K [15].

Experimental

Sample preparation

The starting materials were $CuWO_4$ and RE_2WO_6. Copper tungstate was prepared by heating in air of an equimolar mixture of CuO (99.99%, Aldrich) with WO_3 (99.9%, Fluka). RE_2WO_6 were obtained by solid-state reaction between adequate amounts of RE_2O_3 (RE = Nd, Sm, Eu, Dy, Ho and Er, all oxides with the purity degree of 99.9%, Aldrich) and WO_3. The experimental procedures for preparation of $CuWO_4$ and RE_2WO_6 have been described previously [15–19]. The $CuWO_4/RE_2WO_6$ mixtures (the range of copper tungstate from 20.00 to 90.00 mol%) were heated in air in the following stages: 1023 K (12 h), 1073 K (2 × 12 h), 1098 K (2 × 12 h), 1108 K (2 × 12 h) and 1123 K (3 × 12 h). After each heating stage, the samples were cooled to room temperature, weighted, ground and examined for their contents by XRD method. After final heating stage, samples were examined by DTA-TG, IR and EPR methods.

Apparatuses and measurements

X-ray diffraction phase analysis of the samples was performed using a DRON-3 diffractometer ($CoK_{\alpha\ aver.}$ radiation, $\lambda = 0.179021$ nm, Fe filter). The scans were performed in the 2θ range from 12° to 52° (in step 0.02° and 1 s/step).

DTA-TG examinations were recorded with a Mettler Toledo TGA/SDTA 851 apparatus. These measurements were carried out within the temperature range 298–1323 K, in air (air flow 15 mL min^{-1}), using corundum crucibles and at the heating rate of 2, 5 and 10 K min^{-1}. The mass of each sample was ~50 mg.

The IR spectra were recorded on a Specord M-80 spectrometer. The samples were pressed in pellets with KBr in the mass ratio of 1:100.

The EPR measurements were preformed with a conventional X-band Brücker ELEXSYS E500 CW spectrometer operating at 9.5 GHz with 100 kHz magnetic field modulation. Samples of all compounds (~30 mg) were placed into 4 mm diameter quartz tubes. The first

Table 1 Contents of $CuWO_4/RE_2WO_6$ mixtures and results of XRD analysis of samples obtained after the final heating stage

No.	RE_2WO_6 content in $CuWO_4/RE_2WO_6$ mixture (mol%)	Identified phases RE = Nd	Identified phases RE = Sm, Eu	Identified phases RE = Dy, Ho, Er
1	10.00	$CuNd_2W_2O_{10}$, $CuWO_4$	$Cu_3RE_2W_4O_{18}$, $CuWO_4$	$Cu_3RE_2W_4O_{18}$, $CuWO_4$
2	15.00			
3	20.00			
4	23.00		$Cu_3RE_2W_4O_{18}$, $CuWO_4$[a]	$Cu_3RE_2W_4O_{18}$, $CuWO_4$[a]
5	24.00		$Cu_3RE_2W_4O_{18}$, $CuWO_4$[a]	$Cu_3RE_2W_4O_{18}$, $CuWO_4$[a]
6	25.00		**$Cu_3RE_2W_4O_{18}$**	**$Cu_3RE_2W_4O_{18}$**
7	26.00		$Cu_3RE_2W_4O_{18}$, $CuRE_2W_2O_{10}$[b]	$Cu_3RE_2W_4O_{18}$, RE_2WO_6[c]
8	27.5		$Cu_3RE_2W_4O_{18}$, $CuRE_2W_2O_{10}$[b]	$Cu_3RE_2W_4O_{18}$, RE_2WO_6
9	30.00		$Cu_3RE_2W_4O_{18}$, $CuRE_2W_2O_{10}$	
10	31.00			
11	32.50			
12	35.00			
13	40.00	$CuNd_2W_2O_{10}$, $CuWO_4$[a]		
14	50.00	**$CuNd_2W_2O_{10}$**	**$CuRE_2W_2O_{10}$**	
15	55.00	$CuNd_2W_2O_{10}$, Nd_2WO_6	$CuRE_2W_2O_{10}$, RE_2WO_6	
16	60.00			
17	66.67			
18	80.00			

[a] $CuWO_4$ was identified in a small amount (very small intensities of $CuWO_4$ diffraction lines)

[b] $CuRE_2W_2O_{10}$ was identified in a small amount (very small intensities of $CuRE_2W_2O_{10}$ diffraction lines)

[c] RE_2WO_6 was identified in a small amount (very small intensities of RE_2WO_6 diffraction lines)

derivative of the of the power absorption spectra has been recorded as a function of the applied magnetic field. Temperature dependence of the EPR spectra was registered using an Oxford Instruments ESP helium-flow cryostat in the 8–295 K temperature range. Because the lineshape of the EPR lines was complicated, simulation of the EPR spectrum in form of the sum of few EPR lines with Gaussian or Lorentzian lineshape was applied.

Results and discussion

Reactivity of RE_2WO_6 (RE = Nd, Sm, Eu, Dy, Ho and Er) with $CuWO_4$

Table 1 shows the contents of initial $CuWO_4/RE_2WO_6$ mixtures and the results of XRD analysis for the samples obtained after the last heating of these mixtures. The data in Table 1 indicate that initial components of $CuWO_4/RE_2WO_6$ mixtures are not mutually inert in air. These compounds react to give three series of unknown up to now isostructural compounds with the formulas: $Cu_3RE_2W_4O_{18}$ (RE = Sm, Eu as well as RE = Dy, Ho, Er) and $CuRE_2W_2O_{10}$ (RE = Nd, Sm, Eu). The obtained compounds are formed in the following reactions:

$$3CuWO_{4(s)} + RE_2WO_{6(s)} = Cu_3RE_2W_4O_{18(s)} \quad (4)$$

$$CuWO_{4(s)} + RE_2WO_{6(s)} = CuRE_2W_2O_{10(s)} \quad (5)$$

Characteristic of $Cu_3RE_2W_4O_{18}$ and $CuRE_2W_2O_{10}$ compounds

Crystallography (from powder XRD data)

Powder diffraction patterns of the $Cu_3RE_2W_4O_{18}$ and $CuRE_2W_2O_{10}$ compounds were subjected to a indexing procedure. Diffraction lines recorded within 2θ ($CoK_{\alpha\ aver.}$) 12–52° region were selected for indexing by POWDER program [20, 21]. The results of indexing powder diffraction patterns of the obtained phases are presented in Tables 2, 3, 4. The calculated parameters of unit cells, the values of experimental (obtained by degassing of samples and hydrostatic weighing in pycnometric liquid—CCl_4) and calculated density are tabulated in Table 5. This table shows also unit cells parameters for $CuGd_2W_2O_{10}$ and $Cu_3Gd_2W_4O_{18}$ [15]. Figure 1 shows the powder diffraction patterns of the $Cu_3Eu_2W_4O_{18}$ and $Cu_3Dy_2W_4O_{18}$ phases. As it is seen from Fig. 1 the number and positions of the diffraction lines recorded within 2θ angle range 12–52° for $Cu_3Eu_2W_4O_{18}$ are very different in comparison to the number and positions of the diffraction lines observed in the $Cu_3Dy_2W_4O_{18}$ diffraction pattern. In spite of an identical type of chemical formula it is suggested that $Cu_3RE_2W_4O_{18}$ (RE = Dy, Ho, Er) are not isostructural with the $Cu_3RE_2W_4O_{18}$ (RE = Sm, Eu) compounds.

Thermal properties

Figure 2 shows DTA-TG curves of $CuWO_4$. Two endothermic effects with their onsets at: 1208 and 1236 K were recorded on the DTA curve of copper tungstate. The observed effects are accompanied by the mass losses:

Table 2 Results of indexing $Cu_3RE_2W_4O_{18}$ (RE = Sm, Eu) powder diffraction patterns

No.	$Cu_3\mathbf{Sm}_2W_4O_{18}$			$Cu_3\mathbf{Eu}_2W_4O_{18}$			h	k	l
	d_{obs}/Å	d_{cal}/Å	I/I_0	d_{obs}/Å	d_{cal}/Å	I/I_0			
1	6.1339	6.1338	6	6.1201	6.1205	6	0	0	1
2	5.7276	5.7287	4	5.7125	5.7094	4	1	0	0
3	5.6589	5.6578	19	5.6503	5.6472	16	0	1	1
4	5.4568	5.4606	3	5.4403	5.4426	3	0	$\bar{2}$	1
5	5.3946	5.3957	14	5.3784	5.3791	12	1	1	0
6	5.0639	5.0638	4	5.0449	5.0443	4	1	$\bar{2}$	0
7	4.9182	4.9191	4	4.9095	4.9099	4	0	2	1
8	4.7873	4.7864	35	4.7726	4.7724	34	1	2	0
9	4.3931	4.3941	33	4.3844	4.3823	24	1	2	$\bar{1}$
10	4.0090	4.0096	6	3.9942	3.9945	4	0	$\bar{4}$	1
11	3.9355	3.9353	3	3.9242	3.9239	3	1	3	$\bar{1}$
12	3.6223	3.6220	2	3.6091	3.6084	2	1	$\bar{2}$	1
13	3.5698	3.5683	29	3.5582	3.5582	28	1	4	0
14	3.3961	3.3965	5	3.3825	3.3830	4	1	$\bar{3}$	1
15	3.1984	3.1996	100	3.1892	3.1891	100	0	6	0
16	3.0983	3.0991	21	3.0898	3.0902	20	1	5	0
17	3.0481	3.0471	74	3.0407	3.0409	71	1	1	$\bar{2}$
18	2.9575	2.9583	12	2.9522	2.9503	11	1	$\bar{5}$	$\bar{1}$
19	2.8739	2.8728	40	2.8620	2.8618	37	1	$\bar{6}$	0
20	2.7786	2.7791	2	2.7704	2.7708	2	1	$\bar{2}$	$\bar{1}$
21	2.7449	2.7425	8	2.7355	2.7335	9	0	7	0
22	2.7304	2.7303	62	2.7211	2.7213	45	0	$\bar{4}$	2
23	2.6792	2.6791	10	2.6690	2.6689	9	2	$\bar{3}$	0
24	2.6263	2.6267	47	2.6196	2.6192	48	2	3	$\bar{1}$
25	2.5385	2.5377	4	2.5282	2.5282	3	1	$\bar{7}$	0
26	2.4589	2.4595	20	2.4537	2.4550	15	0	4	2
27	2.3887	2.3896	4	2.3812	2.3814	3	1	$\bar{3}$	2
28	2.3687	2.3696	5	2.3594	2.3604	5	2	$\bar{5}$	0
29	2.3197	2.3230	7	2.3147	2.3156	6	2	$\bar{5}$	$\bar{1}$
30	2.2977	2.2993	3	2.2894	2.2904	2	2	$\bar{3}$	1
31	2.2409	2.2408	7	2.2363	2.2356	6	2	$\bar{3}$	2
32	2.1901	2.1905	5	2.1819	2.1821	4	1	$\bar{5}$	2
33	2.1644	2.1646	6	2.1585	2.1582	5	1	8	0
34	2.1197	2.1203	2	2.1140	2.1141	4	1	$\bar{8}$	$\bar{1}$
35	2.1040	2.1033	1	2.0992	2.0992	1	1	0	$\bar{3}$
36	2.0974	2.0972	6	2.0930	2.0930	6	0	6	2

Table 3 Results of indexing Cu$RE_2W_2O_{10}$ (RE = Nd, Sm, Eu) powder diffraction patterns

No.	Cu**Nd**$_2$W$_2$O$_{10}$			Cu**Sm**$_2$W$_2$O$_{10}$			Cu**Eu**$_2$W$_2$O$_{10}$			h	k	l
	d_{obs}/Å	d_{cal}/Å	I/I_0	d_{obs}/Å	d_{cal}/Å	I/I_0	d_{obs}/Å	d_{cal}/Å	I/I_0			
1	5.8436	5.8419	17	5.7947	5.7907	16	5.7921	5.7869	18	0	1	0
2	5.5265	5.5246	4	5.4856	5.4837	3	5.4747	5.4715	3	2	0	0
3	4.8951	4.8902	10	4.8564	4.8528	9	4.8547	4.8466	11	0	1	2
4	4.8791	4.8781	12	4.8496	4.8431	13	4.8344	4.8352	13	1	1	1
5	4.4322	4.4327	7	4.4284	4.4173	5	4.3955	4.4002	4	2	0	2
6	4.5151	4.0140	3	3.9937	3.9979	4	3.9776	3.9757	4	2	1	0
7	3.7099	3.7103	6	3.6789	3.6768	5	3.6717	3.6715	5	3	0	$\bar{1}$
8	3.5506	3.5497	5							0	1	4
9	3.3459	3.3473	100	3.3105	3.3109	100	3.3089	3.3094	100	3	0	$\bar{3}$
10	3.2770	3.2762	95	3.2540	3.2607	90	3.2504	3.2515	95	1	1	4
11	3.1831	3.1839	69	3.1727	3.1694	82	3.1591	3.1597	81	2	1	3
12	3.1522	3.1481	48							2	1	$\bar{4}$
13	3.0114	3.0102	6	2.9846	2.9905	13	2.9833	2.9835	14	3	1	1
14	2.9788	2.9796	33	2.9616	2.9646	15	2.9562	2.9566	15	0	0	6
15	2.9551	2.9552	26	2.9446	2.9449	34	2.9337	2.9335	29	3	0	3
16	2.9049	2.9043	60							3	1	$\bar{3}$
17				2.8978	2.8953	62	2.8951	2.8934	59	0	2	0
18	2.8133	2.8143	6	2.7894	2.7874	8	2.7875	2.7856	6	2	1	$\bar{5}$
19				2.7701	2.7722	7	2.7634	2.7624	6	1	0	6
20				2.7518	2.7531	7	2.7501	2.7508	9	0	2	2
21	2.7624	2.7623	14	2.7421	2.7419	12	2.7328	2.7357	15	4	0	0
22	2.7483	2.7488	11							4	0	$\bar{2}$
23	2.7086	2.7092	6							3	1	$\bar{4}$
24				2.6945	2.6961	4	2.6921	2.6944	4	1	2	$\bar{2}$
25	2.6596	2.6564	5	2.6358	2.6363	5	2.6323	2.6324	4	1	1	$\bar{6}$
26	2.6244	2.6228	15	2.6037	2.6017	9	2.6046	2.5990	10	0	2	3
27				2.5367	2.5362	26	2.5271	2.5275	17	2	1	5
28	2.5204	2.5176	23							1	2	3
29	2.4502	2.4512	8							2	0	$\bar{7}$
30	2.4323	2.4318	10	2.4163	2.4158	11	2.4098	2.4099	12	4	1	1
31	2.3516	2.3500	30	2.3353	2.3343	26	2.3351	2.3302	30	1	2	4
32				2.3250	2.3269	24	2.3219	2.3214	21	0	1	7
33				2.3178	2.3175	7	2.3108	2.3109	7	4	1	2
34	2.3168	2.3153	20							2	2	3
35	2.3072	2.3065	8							4	1	$\bar{4}$
36							2.2466	2.2416	4	3	2	$\bar{2}$
37	2.2468	2.2458	15	2.2320	2.2289	16	2.2314	2.2254	14	3	2	1
38	2.2017	2.2008	9							3	2	$\bar{3}$
39				2.1940	2.1935	9	2.1904	2.1886	9	5	0	0
40				2.1665	2.1652	4	2.1630	2.1609	5	1	2	5
41							2.1224	2.1186	2	1	0	8
42				2.0706	2.0701	3				1	2	$\bar{6}$
43				2.0646	2.0646	7	2.0592	2.0600	6	3	2	3
44	2.0620	2.0627	4							2	1	7

Table 4 Results of indexing $Cu_3RE_2W_4O_{18}$ (RE = Dy, Ho, Er) powder diffraction patterns

No.	$Cu_3\mathbf{Dy}_2W_4O_{18}$			$Cu_3\mathbf{Ho}_2W_4O_{18}$			$Cu_3\mathbf{Er}_2W_4O_{18}$			h	k	l
	d_{obs}/Å	d_{cal}/Å	I/I_0	d_{obs}/Å	d_{cal}/Å	I/I_0	d_{obs}/Å	d_{cal}/Å	I/I_0			
1	5.6620	5.6602	10	5.6527	5.6527	10	5.6405	5.6379	11	1	0	0
2	5.5382	5.5402	3	5.5265	5.5229	5	5.5177	5.5125	3	1	0	1
3	5.3667	5.3540	6	5.3640	5.3629	6	5.3529	5.3409	6	1	0	$\bar{2}$
4	5.0176	5.0182	2	5.0128	5.0145	1	5.0031	4.9980	2	1	1	$\bar{1}$
5	4.8928	4.8957	4	4.8791	4.8670	2	4.8700	4.8624	2	1	0	3
6	4.4873	4.4948	3	4.4643	4.4650	4	4.4586	4.4616	4	1	0	4
7	4.3711	4.3715	18	4.3657	4.3559	11	4.3476	4.3428	12	0	0	7
8	4.2731	4.2706	10	4.2679	4.2771	11	4.2506	4.2576	9	1	1	$\bar{4}$
9	4.1028	4.1028	1	4.0758	4.0739	3	4.0695	4.0710	3	1	0	5
10	4.0120	4.0119	7	3.9983	3.9986	6	3.9832	3.9878	3	1	0	2
11	3.9877	3.9873	8	3.9771	3.9776	7	3.9607	3.9653	6	1	2	$\bar{1}$
12	3.7415	3.7410	50	3.7138	3.7140	57	3.7099	3.7111	60	1	0	6
13	3.5530	3.5537	16	3.5293	3.5287	15	3.5246	3.5253	16	1	1	6
14	3.4659	3.4659	2	3.4412	3.4513	2	3.4379	3.4413	2	0	2	7
15	3.1737	3.1740	100	3.1606	3.1609	100	3.1531	3.1517	100	0	2	8
16	3.1291	3.1289	92	3.1137	3.1145	96	3.1073	3.1067	94	1	3	1
17	3.0207	3.0221	6	3.0147	3.0145	5	3.0029	3.0042	6	1	3	$\bar{3}$
18	2.9821	2.9833	10	2.9780	2.9834	6	2.9673	2.9703	7	1	2	$\bar{7}$
19	2.9551	2.9486	6	2.9518	2.9527	6	2.9389	2.9384	4	1	0	$\bar{9}$
20	2.9341	2.9277	35	2.9278	2.9216	30	2.9167	2.9110	36	1	3	$\bar{4}$
21	2.9182	2.9183	3	2.9064	2.9065	2	2.8971	2.8980	4	0	2	9
22	2.8288	2.8301	6	2.8265	2.8264	6	2.8104	2.8190	6	2	0	0
23	2.8177	2.8114	11	2.8126	2.8124	18	2.7973	2.8018	17	2	0	1
24	2.7208	2.7151	23	2.7167	2.7152	19	2.7025	2.7061	30	2	1	$\bar{2}$
25	2.6898	2.6914	4	2.6858	2.6827	4	2.6720	2.6775	5	2	1	2
26	2.6206	2.6177	21	2.6187	2.6176	16	2.6049	2.6061	22	1	2	$\bar{9}$
27	2.5349	2.5337	30	2.5320	2.5284	28	2.5198	2.5217	34	2	2	0
28	2.4946	2.5020	1	2.4890	2.4890	2	2.4805	2.4829	2	1	4	2
29	2.4850	2.4837	19	2.4733	2.4715	19	2.4650	2.4645	25	0	4	6
30	2.4485	2.4490	14	2.4464	2.4461	12	2.4361	2.4362	12	1	3	$\bar{8}$
31	2.3368	2.3371	8	2.3250	2.3234	8	2.3197	2.3185	6	1	4	5
32	2.3270	2.3269	13	2.3202	2.3179	14	2.3115	2.3110	12	0	2	12
33	2.3096	2.3060	3	2.3077	2.3054	2	2.2977	2.2954	2	1	2	11
34	2.2920	2.2943	4	2.2807	2.2795	4	2.2761	2.2757	4	1	3	9
35	2.2733	2.2749	4	2.2655	2.2628	3	2.2572	2.2565	4	0	5	0
36	2.2356	2.2367	3	2.2293	2.2280	2	2.2227	2.2232	2	2	3	2
37	2.1927	2.1937	2	2.1910	2.1942	2	2.1829	2.1844	2	1	0	13
38	2.1378	2.1353	3	2.1341	2.1386	3	2.1281	2.1288	2	2	2	$\bar{8}$
39	2.1130	2.1160	13	2.1075	2.1073	11	2.1009	2.1011	12	0	3	12
40	2.0904	2.0885	6	2.0896	2.0886	6	2.0797	2.0801	8	2	3	$\bar{6}$

0.55% and 1.52% by mass starting at the same temperatures (Fig. 2, TG curve). Thus, separate samples of $CuWO_4$ were heated in air above the second effect onset, i.e. at 1273 K for 4 h. After heating the samples were quickly cooled to 263 K and examined by the XRD method. The powder diffraction patterns of samples obtained this way contained four sets of diffraction lines. The authors identified the diffraction lines that can be attributed to: $CuWO_4$ [1], Cu_2WO_4 [22, 23] and WO_3 [24]. The last set of reflections cannot be considered to be characteristic for any other known copper tungstates (Cu_3WO_6 [25], $CuWO_{4-x}$ [4]). On the base of the conducted experiments it could be

Table 5 The parameters of $Cu_3RE_2W_4O_{18}$ and $CuRE_2W_2O_{10}$ unit cells and the values of experimental and calculated density

Compound (color)	*a*/Å	*b*/Å	*c*/Å	*α*/°	*β*/°	*γ*/°	*a*/*b*	*c*/*b*	*Z*	*V*/Å^3	$d_{exp.}$/ g cm^{-3}	$d_{cal.}$/ g cm^{-3}	Ref.
Cu_3**Sm**$_2W_4O_{18}$ (brown)	5.9292(3)	19.337(8)	6.3776(3)	95.849(1)	104.49(8)	92.067(6)	0.3066	0.3298	2	702.83(5)	7.09	7.16	This work
Cu_3**Eu**$_2W_4O_{18}$ (brown)	5.9103(0)	19.269(9)	6.3641(5)	95.767(4)	104.55(2)	92.023(4)	0.3067	0.3303	2	696.63(3)	7.21	7.24	This work
Cu_3**Gd**$_2W_4O_{18}$ (brown)	5.8948(1)	19.216(9)	6.3478(7)	95.757(2)	104.61(4)	92.031(3)	0.3068	0.3303	2	690.93(2)	7.30	7.35	[15]
Cu**Nd**$_2W_2O_{10}$ (grey)	11.156(7)	5.8418(9)	18.051(5)		97.965(4)		1.9098	3.0900	6	1165.1(8)	7.56	7.52	This work
Cu**Sm**$_2W_2O_{10}$ (grey)	11.062(1)	5.7906(9)	17.941(2)		97.499(1)		1.9103	3.0983	6	1139.4(3)	7.80	7.80	This work
Cu**Eu**$_2W_2O_{10}$ (grey)	11.042(9)	5.7868(5)	17.901(8)		97.716(6)		1.9083	3.0935	6	1133.6(3)	7.90	7.87	This work
Cu**Gd**$_2W_2O_{10}$ (grey)	11.021(1)	5.7850(5)	17.874(1)		98.062(7)		1.9051	3.0897	6	1128.3(5)	7.98	8.00	[15]
Cu_3**Dy**$_2W_4O_{18}$ (brown)	5.6621(1)	11.374(5)	30.610(7)		91.485(9)		0.4978	2.6912	6	1970.7(8)	7.70	7.78	This work
Cu_3**Ho**$_2W_4O_{18}$ (brown)	5.6563(3)	11.314(2)	30.510(3)		92.041(7)		0.4999	2.6966	6	1951.3(3)	7.83	7.88	This work
Cu_3**Er**$_2W_4O_{18}$ (brown)	5.6407(1)	11.282(7)	30.414(8)		91.795(5)		0.4999	2.6957	6	1934.7(2)	7.94	7.97	This work

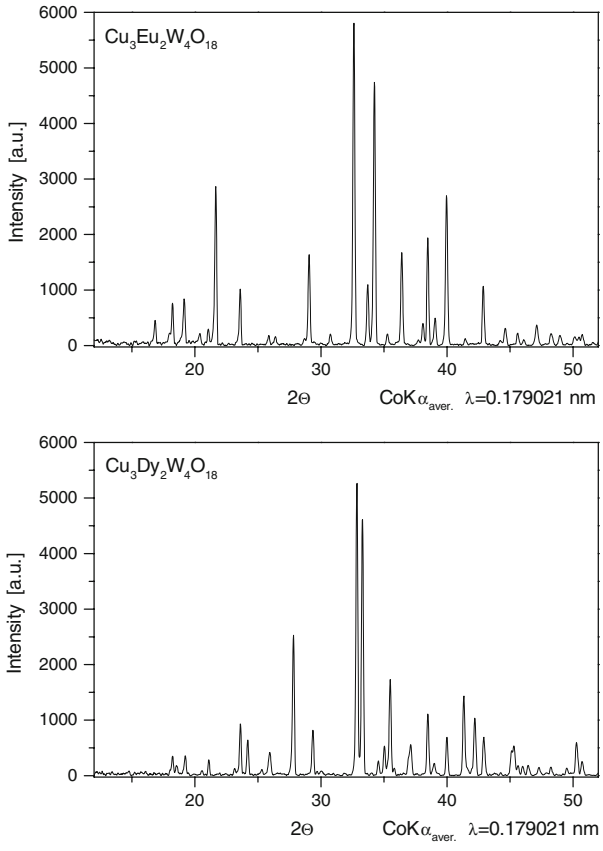

Fig. 1 Powder diffraction patterns of $Cu_3Eu_2W_4O_{18}$ and $Cu_3Dy_2W_4O_{18}$ compounds

suggested that $CuWO_4$ starts to decompose in air at 1208 K. This process is connected with liberation of oxygen and a formation of an unknown copper tungstate—a phase with a deficit of oxygen. The endothermic effect starting at 1236 K is probably associated with decomposition of the latter phase to Cu_2WO_4, WO_3 and an oxygen. The calculated value of mass loss for a $CuWO_4$ decomposition running to Cu_2WO_4, WO_3 and oxygen equals 2.57% by mass. On the other hand the total experimental mass loss recorded during DTA-TG studies is 2.07% by mass. The experimental value is lower than the calculated one and it means that the decomposition process of $CuWO_4$ has not been finished under DTA-TG conditions. It follows that the determination of decomposition manner of $CuWO_4$ needs additional investigations. The intermediate product of $CuWO_4$ decomposition will be studied by XRD, EPR and XPS methods. Results of these examinations will be presented in the following paper.

Figures 3, 4, 5 show the DTA curves of all obtained compounds. On each from the DTA curves of $CuRE_2W_2O_{10}$ (RE = Nd, Sm, Eu, Fig. 3) one endothermic effect was recorded. Two endothermic effects were recorded on each from the DTA curves of $Cu_3RE_2W_4O_{18}$ (RE = Sm, Eu, Fig. 4). On the other hand on each from the DTA curves of the $Cu_3RE_2W_4O_{18}$ (RE = Dy, Ho, Er, Fig. 5) compounds three endothermic effects were observed. No mass losses were recorded on the TG curves (not presented) up to the onsets of the first observed effects on the DTA curves. On the base of DTA studies for

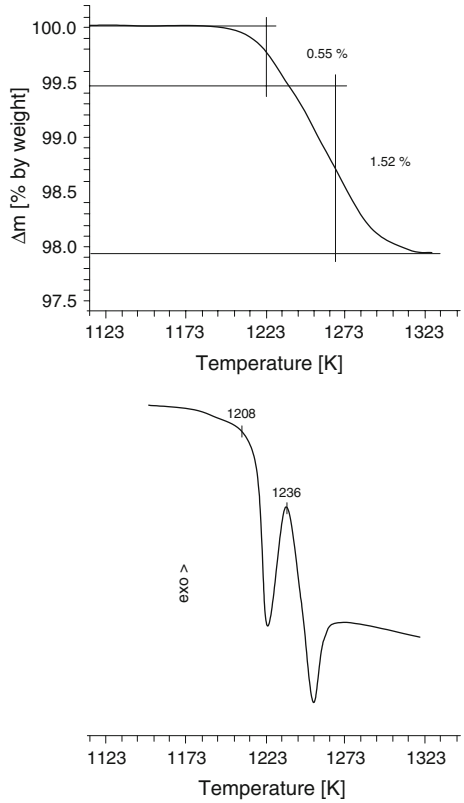

Fig. 2 DTA-TG curves of $CuWO_4$

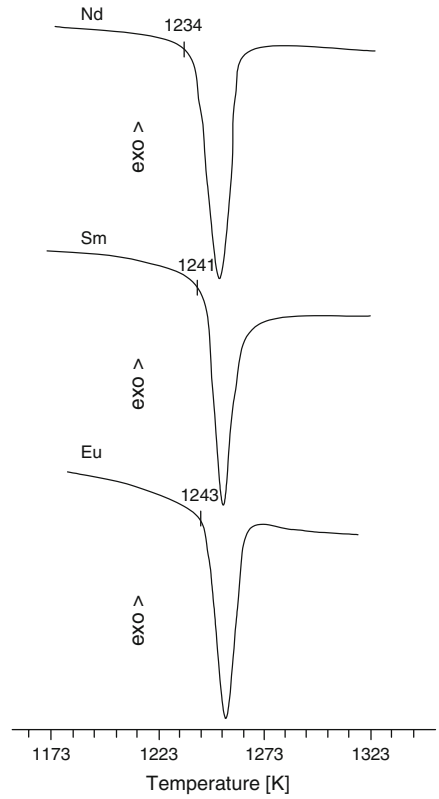

Fig. 3 DTA curves of $CuRE_2W_2O_{10}$ compounds (RE = Nd, Sm, Eu)

$CuRE_2W_2O_{10}$ and observations of the residues obtained after the DTA-TG experiments it was found that the effects with their onsets at: 1234 K(*Nd*); 1241 K(*Sm*); 1243 K(*Eu*) (Fig. 3) were connected with melting of these phases. Consequently, separate samples of $CuRE_2W_2O_{10}$ were heated above their melting points, i.e. at 1248 K(*Nd*); 1253 K (*Sm* and *Eu*) for 4 h and then rapidly removed from a furnace and quenched to 263 K. The results of XRD analysis for the samples obtained in this way showed that they contained the corresponding RE_2WO_6. The incongruent melting of the $CuRE_2W_2O_{10}$ compounds could be described by the Eq. 6 analogously to the melting of $CuGd_2W_2O_{10}$ [15]:

$$CuRE_2W_2O_{10(s)} \rightarrow RE_2WO_{6(s)} + \text{liquid} \quad (6)$$

The first endothermic effects observed on the DTA curves of the $Cu_3RE_2W_4O_{18}$ phases (RE = Sm, Eu; Fig. 4) with their onsets at: 1156 K(*Sm*) and 1163 K(*Eu*) are characterized by melting of these compounds. The melting behavior of $Cu_3RE_2W_4O_{18}$ was also confirmed by XRD method. As in a case of $CuRE_2W_2O_{10}$, samples of the $Cu_3RE_2W_4O_{18}$ phases were heated above their melting point, i.e. at 1168 K(*Sm*) and 1178 K(*Eu*) for 4 h and then quickly quenched. On the base of XRD method it was found

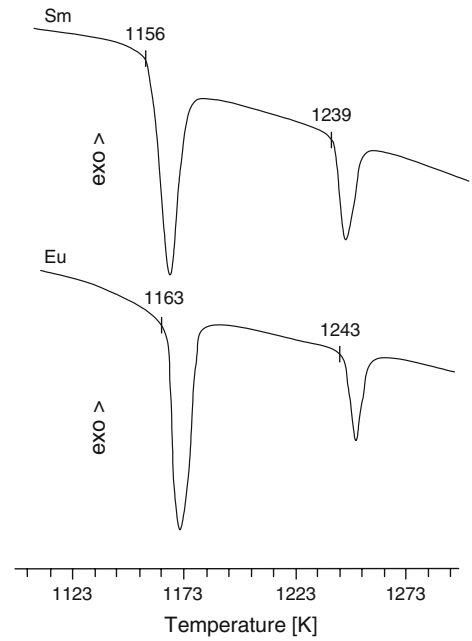

Fig. 4 DTA curves of $Cu_3RE_2W_4O_{18}$ compounds (RE = Sm, Eu)

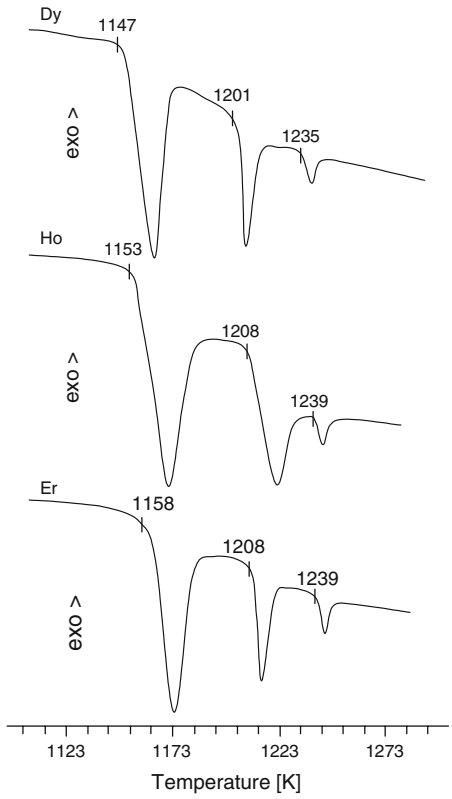

Fig. 5 DTA curves of $Cu_3RE_2W_4O_{18}$ compounds (RE = Dy, Ho, Er)

that the $Cu_3RE_2W_4O_{18}$ samples obtained this way contained an adequate $CuRE_2W_2O_{10}$. Thus, the incongruent melting of $Cu_3RE_2W_4O_{18}$ could be described by the following reaction (analogously to the melting of $Cu_3Gd_2W_4O_{18}$ [15]):

$$Cu_3RE_2W_4O_{18(s)} \rightarrow CuRE_2W_2O_{10(s)} + \text{liquid} \quad (7)$$

The second endothermic effects recorded on the DTA curves of mentioned compounds at: 1239 K(*Sm*) and 1243 K(*Eu*) are associated with melting of $CuRE_2W_2O_{10}$. The endothermic effects recorded on DTA curves of the $Cu_3RE_2W_4O_{18}$ compounds (RE = Dy, Ho, Er, Fig. 5) with their onsets at: 1147 K(*Dy*); 1153 K(*Ho*); 1158 K(*Er*) are due to the melting of these phases. The results of XRD measurements for the "frozen" samples of the $Cu_3RE_2W_4O_{18}$ compounds at: 1163 K(*Dy*); 1173 K(*Ho*); 1178 K(*Er*) showed that they contained $CuWO_4$. The incongruent melting of $Cu_3RE_2W_4O_{18}$ (RE = Dy, Ho, Er) could be described as follows:

$$Cu_3RE_2W_4O_{18(s)} \rightarrow CuWO_{4(s)} + \text{liquid} \quad (8)$$

The effects starting at: 1201 and 1235 K(*Dy*); 1208 and 1239 K (*Ho*, *Er*) (Fig. 4) correspond to decomposition of $CuWO_4$.

Infrared spectra

Figures 6, 7, 8 show IR spectra of the $Cu_3RE_2W_4O_{18}$ (RE = Sm, Eu, Fig. 6), $CuRE_2W_2O_{10}$ (RE = Nd, Sm, Eu, Fig. 7) and $Cu_3RE_2W_4O_{18}$ (RE = Dy, Ho, Er, Fig. 8) compounds. In the light of literature information [26] the absorption bands observed in the IR spectra of $Cu_3RE_2W_4O_{18}$ with their maxima at: 948 and 936 cm^{-1} (*Sm*, *Eu*); 956, 948 and 936 cm^{-1} (*Dy*); 950 and 938 cm^{-1} (*Ho*); 948 and 939 cm^{-1} (*Er*) could be due to the symmetric stretching modes of W–O bonds in isolated structural elements $(W_4O_{16})^{8-}$. This structural element is characteristic for ternary rare-earth tungstates: $KRE(WO_4)_2$ [27–32], $RbRE(WO_4)_2$ [33–35] $AgRE(WO_4)_2$ [36], $CuRE_2W_2O_8$ [37–44] and the stretching vibrations of short terminal W–O bonds in isolated groups of octahedra $(W_4O_{16})^{8-}$ were observed in the infrared spectra of these compounds (the regions of vibration frequencies 950–940 cm^{-1} or 975–950 cm^{-1}) [26]. However, the absorption bands in the IR spectra of the $CuRE_2W_2O_{10}$ compounds with their maxima at: 872 cm^{-1} (*Nd*); 874 cm^{-1} (*Sm*); 876 cm^{-1} (*Eu*) could be related to the stretching modes of W–O bonds in joint WO_6 octahedra by oxygen bridges (three bridges per octahedron) forming structural elements $[(W_2O_9)^{6-}]^{\infty}$ [26, 45]. This element was found in structures of the $RE_2W_2O_9$

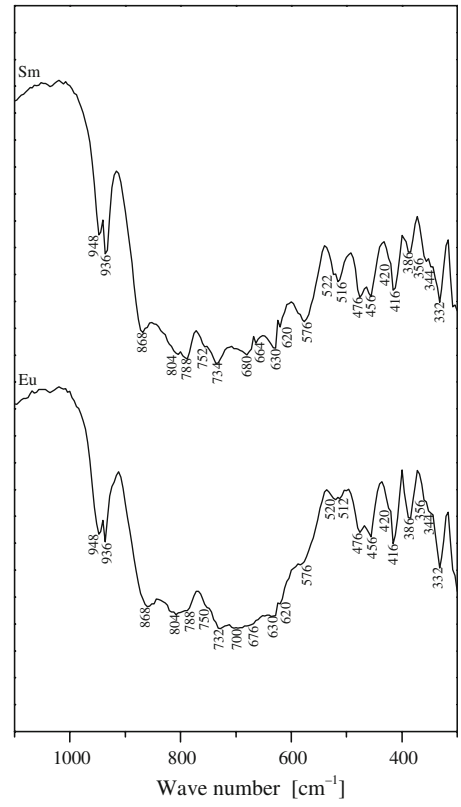

Fig. 6 IR spectra of $Cu_3RE_2W_4O_{18}$ compounds (RE = Sm, Eu)

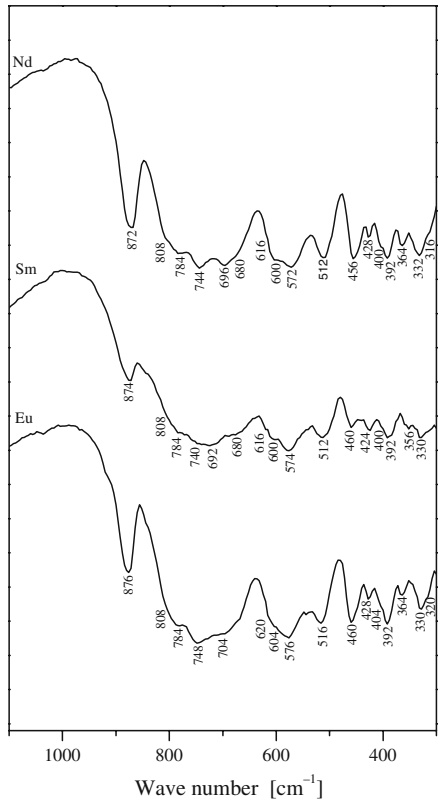

Fig. 7 IR spectra of $CuRE_2W_2O_{10}$ compounds (RE = Nd, Sm, Eu)

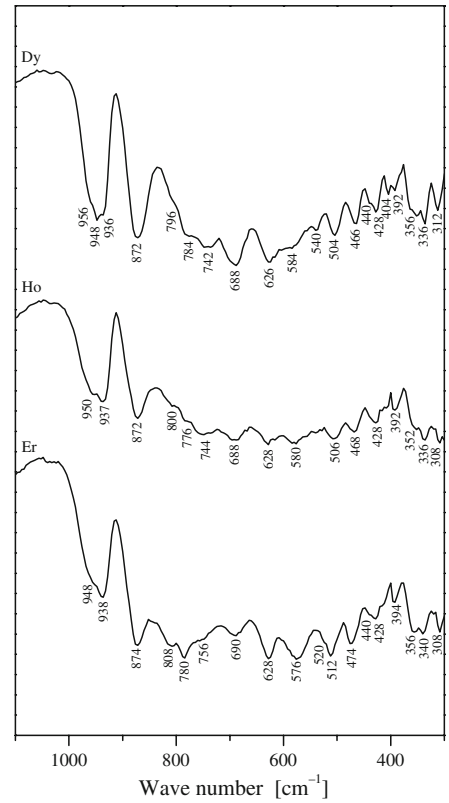

Fig. 8 IR spectra of $Cu_3RE_2W_4O_{18}$ compounds (RE = Dy, Ho, Er)

phases (RE = Pr, Nd, Sm–Gd) [46] and the stretching vibrations of W–O bonds in the structural element $[(W_2O_9)^{6-}]^{\infty}$ were observed in the infrared spectra of these compounds (the regions of vibration frequencies 885–867 cm^{-1}) [26, 45]. The several absorption bands in the frequencies regions: 808–680 cm^{-1} ($CuRE_2W_2O_{10}$, Fig. 7), 868–576 cm^{-1} ($Cu_3RE_2W_4O_{18}$ where RE = Sm, Eu; Fig. 6) and 874–576 cm^{-1} ($Cu_3RE_2W_4O_{18}$ where RE = Dy–Er; Fig. 8) could be due to the asymmetric stretching vibrations of W–O bonds in joint WO_6 octahedra and also to the oxygen double bridge bonds WOOW [45, 47–50]. On the base of literature information [45, 47–50] the absorption bands found in the IR spectra of all analyzed compounds below: 516 cm^{-1} ($CuRE_2W_2O_{10}$), 522 cm^{-1} ($Cu_3RE_2W_4O_{18}$ where RE = Sm, Eu) and 540 cm^{-1} $Cu_3RE_2W_4O_{18}$ where RE = Dy–Er) could be assigned to the symmetric and also asymmetric deformation modes of W–O bonds in joint WO_6 octahedra as well as to the deformation modes of the oxygen bridges WOOW.

EPR spectra

The registered complicated EPR spectra of $Cu_3Ho_2W_4O_{18}$, $CuNd_2W_2O_{10}$, $Cu_3Dy_2W_4O_{18}$, and $Cu_3Er_2W_4O_{18}$ were simulated by the sum of few lines with Gaussian or Lorentzian lineshape. Since the width of the EPR signal ΔH was often comparable with the value of the resonance field H_r, the fitting function $f(H)$ has to include Lorentzian absorption derivatives corresponding to both, right and left circularly polarized components $A(H_+)$ and $A(H_-)$ of the linearly polarized microwave field [51]:

$$f(H) = A(H_+) + A(H_-)$$

$$A(H_\pm) = \frac{16ah_\pm}{\left(3 + h_\pm^2\right)^2}$$

Here, $h_\pm = 2(H \mp H_r)/\Delta H$, and a is the amplitude of the Lorentzian absorption signal. From the fits the values of the resonance field H_r, linewidth ΔH and the integrated intensity $I = a \cdot \Delta H^2$ were calculated.

In Fig. 9 (left panel) the EPR spectra of $Cu_3Ho_2W_4O_{18}$ registered at several temperatures are presented. A very broad and intense line is observed below 30 K. Only defect, not bulk centers attributed to the Cu^{2+} ions are visible. Two different Lorentzian lines were needed: one centered at zero magnetic field and the other at $g \sim 0.90$. As an example of the fitting presented in Fig. 9, left panel, the experimental and fitted spectra at $T = 8.4$ K are presented. In Fig. 9 (right panel) the temperature dependence of integrated intensity and the reciprocal of integrated intensity is shown. In this case the calculated points do not

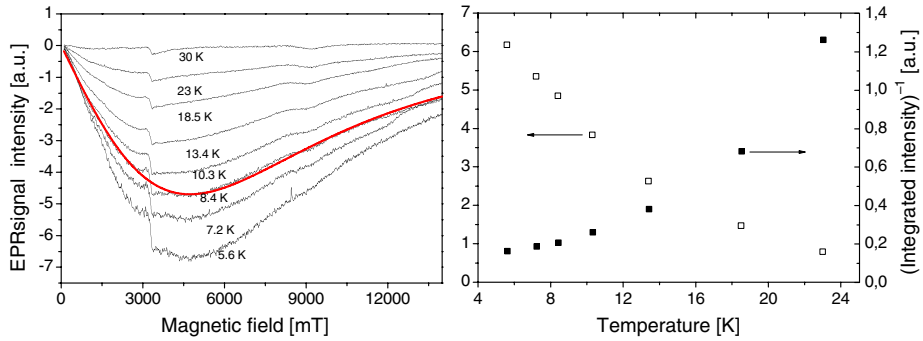

Fig. 9 EPR spectra of $Cu_3Ho_2W_4O_{18}$ at several temperatures (*left panel*) and experimental (*fat*) and fitted (*thin*) spectrum at $T = 8.4$ K (*solid line*). *Right* panel: temperature dependence of the EPR integrated intensity (*left axis*, *open squares*) and reciprocal of integrated intensity (*right axis*, *filled squares*)

seem to follow the Curie–Weiss law, $I(T) \sim 1/(T - T_{CW})$. Trivalent holmium ($4f^{10}$) is a non-Kramers ion with the $^5I_8$ ground term that in a sufficiently low symmetry is split by the crystal field into singlet levels. In that situation no EPR line is expected to be registered by conventional X-band spectrometer. Thus, the signal that is observed in $Cu_3Ho_2W_4O_{18}$ might be due to the temperature change of Q-factor of the resonance cavity containing the investigated powder sample.

In Fig. 10 (upper panel) several EPR spectra of $CuNd_2W_2O_{10}$ registered at different temperatures are presented. Only one broad Lorentzian line was sufficient to obtain satisfactory fit to the experimental spectrum. The integrated intensity (Fig. 10, left lower panel) of the EPR spectrum of $CuNd_2W_2O_{10}$ follows the Curie–Weiss law with $T_{CW} = 1.9(3)$ K indicating on the presence of a weak ferromagnetic interaction. Temperature dependence of linewidth and g-factor of that line (Fig. 10, right lower panel) reveal that below 10 K the linewidth and g-factor decrease slowly with temperature increase, but above 10 K the trend is reversed. Free Nd^{3+} ion has a $4f^3$ configuration with $^4I_{9/2}$ ground state. In a crystal field of tetragonal or lower symmetry the $^4I_{9/2}$ manifolds splits into five Kramers doublets. At liquid helium temperature only the lowest doublet is populated, therefore the system could be described as a fictitious spin $S = 1/2$. Although the calculated value of the g-factor is reasonable for the Nd^{3+} ion, the similarity of the registered spectrum to previously

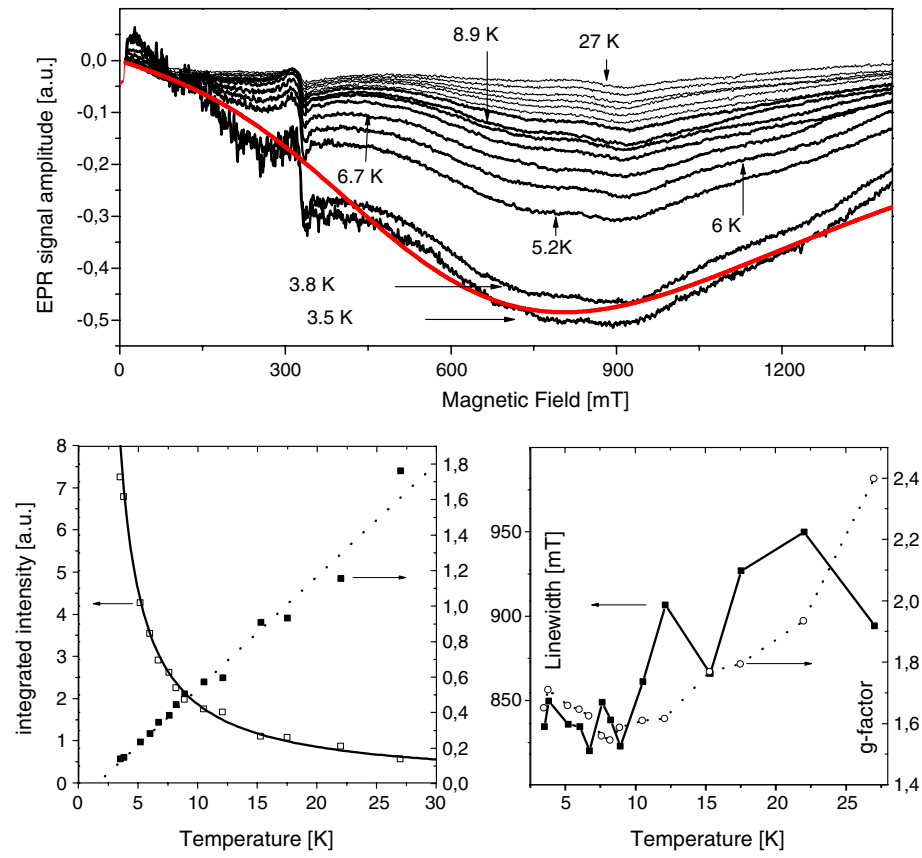

Fig. 10 *Upper panel*—EPR spectra of $CuNd_2W_2O_{10}$ at several temperatures and experimental (*fat*) and fitted (*thin*) spectrum at $T = 3.5$ K (*solid line*); *left lower panel*—temperature dependence of the EPR integrated intensity (*left axis*, *open squares*) and reciprocal of integrated intensity (*right axis*, *filled squares*). The lines are fittings to the Curie–Weiss law; *right lower panel*—temperature dependence of the linewidth (*left axis*, *filled squares*) and g-factor (*right axis*, *open circles*)

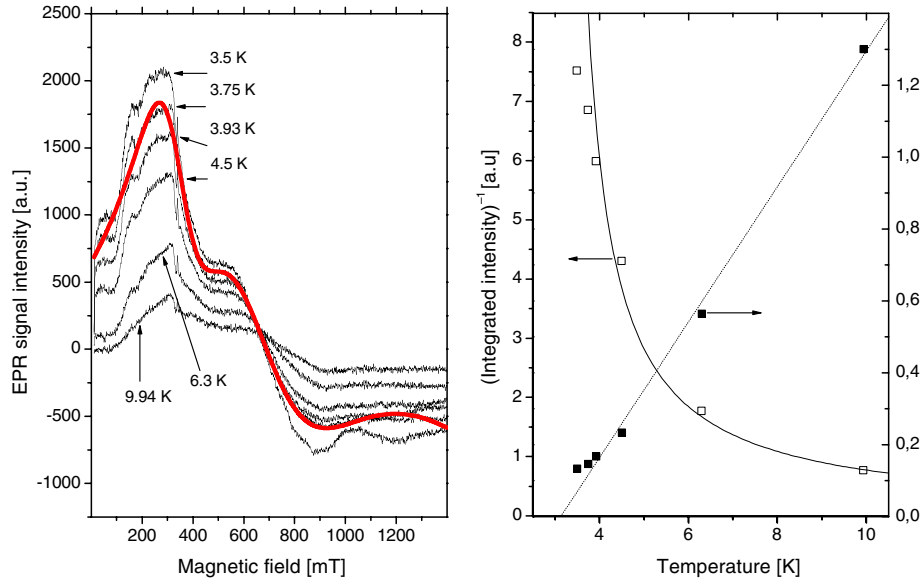

Fig. 11 EPR spectra of $Cu_3Dy_2W_4O_{18}$ at several temperatures (*left panel*) and experimental (*fat*) and fitted (*thin*) spectrum at $T = 3.75$ K (*solid line*). *Right panel*—temperature dependence of the EPR integrated intensity (*left axis*, *open squares*) and reciprocal of integrated intensity (*right axis*, *filled squares*). The *lines* are fittings to the Curie–Weiss law

discussed $Cu_3Ho_2W_4O_{18}$ prevent us to attribute this signal univocally to the neodymium ion.

EPR spectra of the $Cu_3Dy_2W_4O_{18}$ compound at several temperatures are presented in Fig. 11 (left panel). The main, broad component is due probably to the Dy^{3+} ions and could be registered only at temperatures below 20 K. A narrow, weak line near $g \sim 2$ is attributed to Cu^{2+} ions. Taking into account a small amplitude of this line it should be assigned not to bulk Cu^{2+} ions in the $Cu_3Dy_2W_4O_{18}$ structure but to a defect centers involving separate Cu^{2+} ions, appearing e.g. on the surface of the grains. The absence of bulk copper in the EPR spectrum could be explained by a very short relaxation time of the Cu^{2+} subsystem that results in a very broad line (over 2 T) not possible to register by a conventional X-band spectrometer. A similar situation is encountered in case of copper ions in the normal phase of the copper oxides high-temperature superconductors [51]. Dy^{3+} spectrum was simulated by three Lorentzian shaped lines. The calculated g-factors were 0.56, 0.94 and 1.68. Comparison of the experimental and fitted spectra at $T = 3.75$ K is shown in left panel in Fig. 11. In Fig. 11 (right panel) the temperature dependence of the EPR integrated intensity and its reciprocal is shown. Above 4 K that relation is in the form of the Curie–Weiss law, $I(T) \sim 1/(T - T_{CW})$, with $T_{CW} = 3.1(4)$ K. The positive sign of the Curie–Weiss temperature indicate on the presence of ferromagnetic interaction between dysprosium ions. The Kramers ion Dy^{3+}, whose electronic configuration is $4f^9$, has a free-ion ground state of $^6H_{15/2}$. In tetragonal or lower symmetry of crystal field the 16-fold degenerate ground term is split into eight Kramers doublets. The lack of knowledge of the exact point symmetry site of the Dy^{3+} ion unable us to calculate of the lowest crystal field energy levels.

In Fig. 12 (left panel) the registered spectra of the $Cu_3Er_2W_4O_{18}$ compound are shown. Fitting with two Lorentzian lines ($g \sim 2.0$ and 0.86) was necessary to obtain reasonable agreement with the observed spectra. The

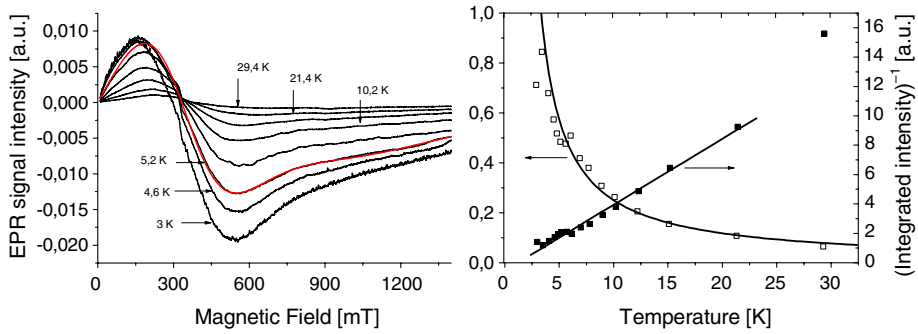

Fig. 12 EPR spectra of $Cu_3Er_2W_4O_{18}$ at several temperatures (*left panel*) and experimental (*fat*) and fitted (*thin*) spectrum at $T = 5.2$ K (*left panel*). *Right panel*—temperature dependence of the EPR integrated intensity (*left axis*, *open squares*) and reciprocal of integrated intensity (*right axis*, *filled squares*). The *lines* are fittings to the Curie–Weiss law

integrated intensity (right panel) followed the Curie–Weiss law with $T_{CW} = 1.5(3)$ K indicating on the presence of ferromagnetic interactions. The electronic configuration of Er^{3+} is $4f^{11}$ with a free-ion ground state of $^4I_{15/2}$. In a cubic crystal field the 16-fold degenerate ground state of the Er^{3+} ion splits into two doublets, Γ_6 and Γ_7, with an effective spin $S = 1/2$ and g value of 6.8 and 6.0, respectively, and into three Γ_8 quartets, each with an effective spin $S = 3/2$, generating an anisotropic Zeeman interaction. In a sufficiently strong low symmetry crystal field the quartets split into doublets. In case of the $Cu_3Er_2W_4O_{18}$ compound the calculated g-factors are very different from those expected for Γ_6 and Γ_7 doublets what might indicate on a relatively large departure from axial symmetry at the Er^{3+} crystal site.

Conclusions

Eight new compounds with the formulas: $Cu_3RE_2W_4O_{18}$ (RE = Sm, Eu as well as RE = Dy, Ho, Er) and $CuRE_2W_2O_{10}$ (RE = Nd, Sm, Eu) were prepared. The latter phases crystallize in the monoclinic system and are isostructural with $CuGd_2W_2O_{10}$ [15]. The $Cu_3RE_2W_4O_{18}$ (RE = Sm, Eu) compounds crystallize in the triclinic system and they are isostructural with $Cu_3Gd_2W_4O_{18}$ [15]. The $Cu_3RE_2W_4O_{18}$ (RE = Dy, Ho, Er) phases crystallize in the monoclinic system. The cell volume of all compounds decreases when rare-earth ion radius decreases (Table 5). The calculated values of the ratios of cell parameters a/b and c/b (Table 5) for respective compounds are: ~0.31 and ~0.33 for $Cu_3RE_2W_4O_{18}$ (RE = Sm, Eu, Gd); ~1.91 and ~3.10 for $CuRE_2W_2O_{10}$ (RE = Nd, Sm, Eu, Gd); ~0.50 and ~2.70 for $Cu_3RE_2W_4O_{18}$ (RE = Dy, Ho, Er). These values could indicate that the obtained compounds had probably a layered structure. All compounds melt incongruently at temperatures below 1273 K. Their melting temperatures insignificantly increase with decreasing radius of the rare-earth ion. Copper tungstate is stable up to 1208 K. It is suggested that the anion lattice of the $Cu_3RE_2W_4O_{18}$ compounds is built from isolated groups of octahedra $(W_4O_{16})^{8-}$, while the anion lattice of the $CuRE_2W_2O_{10}$ phases is built from joint WO_6 octahedra forming structural elements $[(W_2O_9)^{6-}]^{\infty}$. The observed EPR spectra of $Cu_3RE_2W_4O_{18}$ (RE = Dy, Ho, Er) and $CuNd_2W_2O_{10}$ compounds consisted of a broad, intense line originating generally from the rare-earth ions and a weak, narrow line ($g \sim 2.0$) from Cu^{2+} centers. The latter centers involve separate Cu^{2+} ions, appearing often on the surface of the grains. The absence of bulk copper in the EPR spectrum is assumed to be due to a very short relaxation time of the Cu^{2+} subsystem that results in a very broad line not registered by a conventional X-band spectrometer, as it was reported previously for high-temperature semiconductors based on copper oxides. This conclusion is additionally confirmed by previous supposition did by authors on a type of structure of the investigated compounds, being layered. The fitting of the experimental spectra with Lorentzian lines revealed that the magnetic anisotropy is the greatest one for Dy^{3+} system in $Cu_3Dy_2W_4O_{18}$ (three different g-factors) and the smallest one for Er^{3+} in $Cu_3Er_2W_4O_{18}$ (one g-factor). In most cases the dominating interaction in the rare earth spin system is ferromagnetic.

Acknowledgements The authors deeply acknowledge to Dr. A. Worsztynowicz for assistance in EPR measurements.

References

1. Kihlborg L, Gebert E. $CuWO_4$, a distorted wolframite-type structure. Acta Crystallogr. 1970;B26:1020–6.
2. Klein S, Weitzel H. PERNOD – a program for refinement of crystal structure parameters from neutron powder diffraction patterns. J Appl Crystallogr. 1975;8:54–9 (in German).
3. Schofield PF, Knight KS, Redfern SAT, Cressey G. Distortion characteristics across the structural phase transition in $(Cu_{1-x}Zn_x)WO_4$. Acta Crystallogr. 1997;B53:102–12.
4. Gebert E, Kihlborg L. On the crystal structure of copper wolframate. Acta Chem Scand. 1967;21:2575–6.
5. Van Uitert LG, Preziosi ST. Zinc tungstates for microwave maser application. J Appl Phys. 1962;33:2908.
6. Gillette RH. Calcium and cadmium tungstate as scintillation counter crystals for gamma-ray detection. Rev Sci Instrum. 1950; 21:294–301.
7. Peter M. Millimeter-wave paramagnetic resonance spectrum of ^6S state impurity (Fe^{3+}) in $MgWO_4$. Phys Rev. 1959;113:801–3.
8. Blasse G, Grabmaier BC. Luminescent materials. Berlin: Springer; 1994.
9. Feldman C, Jüstel T, Ronda CR, Schmidt PJ. Inorganic luminescent materials: 100 years of research and application. Adv Funct Mater. 2003;13:511–4.
10. Hidaka Ch, Yamagishi E, Takizawa T. Photoluminescence spectra of rare earth doped $CaGa_2S_4$ single crystals. J Phys Chem Solids. 2005;66:2058–60.
11. Jabbarov RB, Chartier C, Tagiev BG, Tagiev OB, Musayeva NN, Barthou C, et al. Radiative properties of Eu^{2+} in $BaGa_2S_4$. J Phys Chem Solids. 2005;66:1049–56.
12. Wang Y, Gao H. Photoluminescence of new red phosphor $SrZnO_2:Eu^{3+}$. J Solid State Chem. 2006;179:1870–3.
13. Wang Z, Liang H, Gong M, Su Q. Luminescence investigation of Eu^{3+} activated double molybdates red phosphors with scheelite structure. J Alloys Compd. 2007;432:308–12.
14. Zhao X, Wang X, Chen B, Meng Q, Di W, Ren G, et al. Novel Eu^{3+}-doped red-emitting phosphor $Gd_2Mo_3O_9$ for white-light-emitting-diodes (WLEDs) application. J Alloys Compd. 2007; 433:352–5.
15. Tomaszewicz E, Worsztynowicz A, Kaczmarek SM. Subsolidus phase relations in $CuWO_4$–Gd_2WO_6 system. Solid State Sci. 2007; 9:43–51.
16. Tomaszewicz E. Reactivity in the solid state between $CoWO_4$ and RE_2WO_6 where RE = Sm, Eu, Gd. Thermochim Acta. 2006; 447:69–74.

17. Tomaszewicz E. Synthesis and some properties of new zinc and rare-earth metal tungstates $ZnRE_4W_3O_{16}$. Solid State Sci. 2006;8: 508–12.
18. Tomaszewicz E. New praseodymium(III) and d-electron metals tungstates of the formula $MPr_2W_2O_{10}$ (M = Mn, Co, Cd). J Therm Anal Calorim. 2008;93:711–5.
19. Tomaszewicz E. New cobalt and rare earth metal tungstates $CoRE_2W_2O_{10}$. J Therm Anal Calorim. 2007;90:255–9.
20. Taupin D. General method of indexing powder patterns. J Appl Crystallogr. 1968;1:178–81 (in French).
21. Taupin D. A powder-diagram automatic-indexing routine. J Appl Crystallogr. 1973;6:380–5.
22. Marinder BO, Wang PL, Werner PE, Westdahl M, Andresen AF, Louër D. Powder diffraction studies of Cu_2WO_4. Acta Chem Scand. 1987;A41:152–7.
23. Mumm HC, Müller-Buschbaum Hk. Crystal structure of Cu_2WO_4. J Less-Common Met. 1988;142:85–90 (in German).
24. Woodward PM, Sleight AW, Vogt T. Structure refinement of triclinic tungsten trioxide. J Phys Chem Solids. 1995;56:1305–15.
25. Gebert E, Kihlborg L. The crystal structure of a new copper wolfram oxide, Cu_3WO_6. Acta Chem Scand. 1969;23:221–31.
26. Tsaryuk VI, Zolin VF. Vibration and vibronic spectra of lanthanide compounds with different types of coordination polyhedra of tungsten and molybdenum. Spectrochim Acta. 2001; A57:355–9.
27. Klevtsov PV, Klevtsova RF. Polymorphism of double molybdates and tungstates with the general formula $M^+R^{3+}(EO_4)_2$. Zh Strukt Khim. 1977;18:419–39 (in Russian).
28. Klevtsov PV, Kozeeva LP, Pavlyuk AA. Crystallization and polymorphism of potassium and rare earth molybdates $KLn(MoO_4)_2$ (Ln = La, Ce, Pr and Nd). Kristallografiya. 1975; 20:1216–20 (in Russian).
29. Klevtsov PV, Kozeeva LP, Kharchenko LYu. Investigations of crystallization and polymorphism of potassium and R3+ double tungstates $KR(WO_4)_2$. Kristallografiya. 1975;20:1210–5 (in Russian).
30. Borisov SV, Klevtsova RF. Crystal structure of $KY(WO_4)_2$. Kristallografiya. 1968;13:517–9 (in Russian).
31. Klevtsova RF, Volkova LM. Crystal structure of monoclinic $KNd(WO_4)_2$. Kristallografiya. 1972;17:859–61 (in Russian).
32. Soloveva LP, Borisov SV. Crystal structure of double tungstate (K, Nd)$Nd(WO_4)_2$. Kristallografiya. 1969;14:613–6 (in Russian).
33. Klevtsov PV, Kozeeva LP, Klevtsova RF. Synthesis and polymorphism of rubidiumand lanthanum tungstate $RbLa(WO_4)_2$. Kristallografiya. 1976;21:106–12 (in Russian).
34. Kharchenko LYu, Klevtsov PV. Hydrothermal synthesis of rubidium and rare-earth metal tungstates. Kristallografiya. 1972; 17:694–5 (in Russian).
35. Ipatova EN, Klevtsova RF, Soloveva LP. Crystal structure of rubidium and dysprosium tungstate $RbDy(WO_4)_2$. Kristallografiya. 1976;21:1121–5 (in Russian).
36. Klevtsov PV, Maksin VI, Klevtsova RF, Golub AM. Polymorphism of silver and rare-earth metal tungstates. Kristallografiya. 1976;21:759–65 (in Russian).
37. Boehlke A, Müller-Buschbaum Hk. Crystal structure of $CuLaW_2O_8$ and $CuSmW_2O_8$. J Less-Common Met. 1990;162:141–7 (in German).
38. Müller-Buschbaum Hk, Sedello O. The crystal structures of α-$CuGdW_2O_8$ and $CuNdMo_2O_8$. J Alloys Compd. 1994;204:237–41 (in German).
39. Müller-Buschbaum Hk, Szillat H. The crystal chemistry of copper and rare-earth oxytungstate: (I): triclinic α-$CuTbW_2O_8$, (II): monoclinic-$CuInW_2O_8$ and (III): monoclinic-$CuYW_2O_8$. Z Anorg Allg Chem. 1994;620:642–6 (in German).
40. Müller-Buschbaum Hk, Krüger TF. A contribution on the crystal structure of $CuYW_2O_8$, $CuHoW_2O_8$ and $CuYbW_2O_8$. Z Anorg Allg Chem. 1992;607:52–6 (in German).
41. Müller-Buschbaum Hk, Gressling T. Dimorphism of copper and rare-earth oxotungstates in the example of $CuErW_2O_8$ and $CuDyW_2O_8$. J Alloys Compd. 1993;202:63–7 (in German).
42. Müller-Buschbaum Hk, Gressling T. The crystal structure of β-$CuTmW_2O_8$ and β-$CuLuW_2O_8$. J Alloys Compd. 1993;201:267–70 (in German).
43. Krüger TF, Müller-Buschbaum Hk. The β-$CuNdW_2O_8$, β-Li-YbW_2O_8 and copper and bismuth oxotungstate $CuBiW_2O_8$. J Alloys Compd. 1992;190:L1–3 (in German).
44. Mumm HC, Müller-Buschbaum Hk. Synthesis and structure of a new form of $CuNdW_2O_8$: β-$CuNdW_2O_8$. Z Anorg Allg Chem 1988;566:25–30 (in German).
45. Fomichev VV, Kondratov OI, Gagarina VA, Petrov KI. Investigations of IR spectra of rare-earth metal tungstates with the formula $Ln_2W_2O_9$. Zh Neorg Khim. 1978;23:87–93 (in Russian).
46. Borisov SV, Klevtsova RF. Crystal structure of $Pr_2W_2O_9$. Kristallografiya. 1970;15:38–42 (in Russian).
47. Hanuza J, Mączka M, van der Maas JH. Vibrational properties of double tungstates of the $M^IM^{III}(WO_4)_2$ family (M^I = Li, Na, K; M^{III} = Bi, Cr). J Solid State Chem. 1995;117:177–88.
48. Hanuza J, Macalik L, Mączka M, Lutz ETG, van der Maas JH. Vibrational characteristics of the double oxygen bridge in the $NaIn(WO_4)_2$ and $NaSc(WO_4)_2$ tungstates with wolframite structure. J Mol Struct. 1999;511–512(8):8–106.
49. Daturi M, Busca G, Borel MM, Leclaire A, Piaggio P. Vibrational and XRD study of the system $CdWO_4$–$CdMoO_4$. J Phys Chem. 1997;B101:4358–69.
50. Mączka M. Vibrational characteristics of the alkali metal–indium double molybdates $M\text{In}(MoO_4)_2$ nd tungstates $M\text{In}(WO_4)_2$ (M = Li, Na, K, Cs). J Solid State Chem. 1997;129:287–97.
51. Abragam A, Bleaney B. Electron paramagnetic resonance of transition ions. Clarendon: Oxford University Press; 1970.